Analytical integration of the heater and sensor 3 ω signals of anisotropic bulk materials and thin films

Jose Ordonez-Miranda, Laurent Jalabert, Yunhui Wu, Sebastian Volz, Masahiro Nomura

RESEARCH ARTICLE | MAY 25 2023

Analytical integration of the heater and sensor 3ω signals of anisotropic bulk materials and thin films

Jose Ordonez-Miranda ; Laurent Jalabert ; Yunhui Wu ; Sebastian Volz ; Masahiro Nomura

J. Appl. Phys. 133, 205104 (2023)
https://doi.org/10.1063/5.0151725
CHORUS

Journal of Applied Physics ARTICLE scitation.org/journal/jap

Analytical integration of the heater and sensor 3ω signals of anisotropic bulk materials and thin films

Cite as: J. Appl. Phys. **133**, 205104 (2023); doi: 10.1063/5.0151725
Submitted: 24 March 2023 · Accepted: 8 May 2023 ·
Published Online: 25 May 2023

Jose Ordonez-Miranda,[1,2,a)] Laurent Jalabert,[1,2] Yunhui Wu,[2] Sebastian Volz,[1,2] and Masahiro Nomura[1,2]

AFFILIATIONS

[1]LIMMS, CNRS-IIS IRL 2820, The University of Tokyo, Tokyo 153-8505, Japan
[2]Institute of Industrial Science, The University of Tokyo, Tokyo 153-8505, Japan

[a)]**Author to whom correspondence should be addressed:** jose.ordonez@cnrs.fr

ABSTRACT

We derive and analytically integrate the models for the heater and sensor 3ω signals of the temperature field of anisotropic bulk materials and thin films. This integration is done by using the Fourier transform and expressing the frequency dependence of temperature in terms of the modified Bessel and Struve functions, which are well-implemented in major computation software. The effects of the radiative losses and interface thermal resistance are also evaluated for different frequency regimes. Further, by fitting the 3ω model integrated over the heater and sensor widths to experimental data recorded up to 31 kHz, the thermal conductivity and thermal diffusivity of a quartz glass wafer are determined for temperatures ranging from 300 to 800 K. The obtained results show that the usual log-linear approximation can induce an uncertainty of about 5% on the thermal conductivity values. The exact integrated models are thus expected to facilitate the accurate determination of the thermal conductivity and thermal diffusivity of anisotropic materials through a wide spectrum of modulation frequencies and without time-consuming numerical integration.

I. INTRODUCTION

The first concept of the 3ω method was developed in 1910 by Corbino,[1] who applied an alternating electrical current to measure the thermal diffusivity of metal filaments. In early 1987, Cahill and Pohl[2] and Birge and Nagel[3] applied this modulated electrical excitation to generate heat and measure the thermal conductivity of amorphous solids and the specific heat of liquids, respectively. In 1990, Cahill[4] further extended its application to measure the thermal conductivity of dielectric solids through the development of the standard 3ω method that is widely applied nowadays. The method takes its name from the measured voltage oscillating with a frequency 3ω due to the circulation of an electrical current modulated with a frequency ω that heats up the sample material through Joule heating.[5] This well-mastered electrical heating represents one of the main advantages of the 3ω method, which has been adapted to measure the thermal conductivity of thin films,[6–10] free-standing membranes,[11,12] nanowires,[13] and nanotubes.[14]

The modulated electrical heating for the 3ω method generates thermal waves, whose propagation distance increases as the modulation frequency decreases. This frequency dependence allows probing the material properties at different penetration depths by recording the real and imaginary parts (or amplitude and phase) of the temperature fluctuations as functions of frequency. The fitting of these 3ω signals to a proper model determines the thermal conductivity and thermal diffusivity of solids. For bulk materials and thin films, the 3ω models are expressed in terms of integrals or approximate expressions valid for either low or high frequencies.[4,7,15–22] A semi-analytical solution of the 3ω model was also derived by Gurrum *et al.*,[23] who showed that the heater thermal conduction could be particularly important for anisotropic materials. More recently, Duquesne *et al.*[24] managed to integrate the 3ω model for a semi-infinite isotropic material and expressed the temperature field in terms of the Meijer-*G* function. They[24] showed that this function is related to a double integral, which allowed them to rigorously derive, for the first time, the low- and high-frequency regimes of the temperature field involving a fundamental mathematical constant (Euler gamma function) that was previously estimated via numerical integration.[6,15,25] As the analytical integration of the 3ω model in terms of easy-to-compute functions can greatly simplify the fitting of experimental data, the

integrated expressions of this model for other material configurations of practical interest are highly desirable, but challenging.

The goal of this work is to derive and analytically integrate the 3ω models for anisotropic bulk materials and thin films. This integration is done by using the Fourier transform and expressing the temperature fields in terms of the modified Bessel and Struve functions, which are well-implemented in major computation software. In contrast with previous works dealing with integral expressions for the 3ω model or its approximate integration for anisotropic materials,[7,9] here we report the exact integrated temperature field of the heater and sensor signals of the 3ω method. Further, the effects of the radiative losses and interface thermal resistance are also discussed for different modulation frequencies.

II. THEORETICAL MODEL

Let us consider an anisotropic thin film deposited on an anisotropic substrate and supporting a two-dimensional heat conduction and radiative losses due to its uniform thermal excitation via a heater pad, as shown in Fig. 1. This heat conduction is driven by the in-plane ($k_{m\parallel}$) and cross-plane ($k_{m\perp}$) thermal conductivities of the film ($m = 1$) and substrate ($m = 2$), while the losses are determined by the emissivity ε of the film inside a vacuum chamber. Under these conditions, the temperature $T(x, y, t)$ distribution of the film and substrate is given by the diffusion equation

$$k_{\parallel}\frac{\partial^2 T}{\partial x^2} + k_{\perp}\frac{\partial^2 T}{\partial y^2} = C\frac{\partial T}{\partial t}, \tag{1}$$

where C is the volumetric heat capacity.

Considering that the heater is uniformly heated with a power $P(t)$ and applying the Stefan–Boltzmann formula for the radiative losses, the solution of Eq. (1) is subject to the continuity of the heat flux and discontinuity of temperature, as follows:

$$-k_{1\perp}\frac{\partial T_1}{\partial y}\Big|_{y=0} + h(T_1|_{y=0} - T_0) = \frac{P(t)}{2ab}H(a - |x|), \tag{2a}$$

$$-k_{1\perp}\frac{\partial T_1}{\partial y}\Big|_{y=d} = -k_{2\perp}\frac{\partial T_2}{\partial y}\Big|_{y=d}, \tag{2b}$$

$$T_1(x, d, t) - T_2(x, d, t) = -Rk_{2\perp}\frac{\partial T_2}{\partial y}\Big|_{y=d}, \tag{2c}$$

$$T_n(-x, y, t) = T_n(x, y, t), \tag{2d}$$

where H is the Heaviside function, R is the interface thermal resistance between the film and substrate set at the respective temperatures T_1 and T_2, and T_0 is the sample room temperature. The substrate is considered to be semi-infinite in thickness (y direction) and length (x direction). The coefficient of radiative losses $h = 4\varepsilon\sigma T_0^3$, with σ being the Stefan–Boltzmann constant, arises from linearizing the Stefan–Boltzmann formula for a temperature difference $T_1 - T_0 \ll T_0$. As this far-field formula is valid when the heater and sensor dimensions are much larger than the peak wavelength of thermal radiation ($> 10\,\mu$m for $T_0 > 300$ K, as established by Wien's law), the definition of $h = 4\varepsilon\sigma T_0^3$ only applies under these conditions. Otherwise, this definition of h fails, but Eq. (2a) remains valid for a generalized coefficient of radiative losses and a film temperature rise small with respect to its room temperature. Further, in the presence of convective losses, Eq. (2a), and hence, the results obtained in this work still apply after replacing h by $h + h_{\text{conv}}$, with h_{conv} being the coefficient of convective losses, as established by the Newton law of cooling. The circulation of an electrical current $I = I_0\cos(\omega t)$ modulated in time t with a frequency ω, along the heater of electrical resistance R_0, generates an electrical power $P(t) = R_0 I^2 = 0.5R_0 I_0^2(1 + \cos(2\omega t))$ that splits into a steady-state component and a temporal one oscillating with a frequency 2ω. For this thermal excitation, the temperature profile predicted by the linear differential Eq. (1) reads

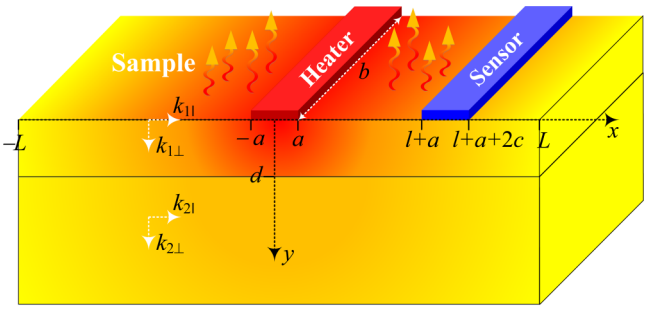

FIG. 1. Scheme of the heater and sensor deposited on a thin film to determine its thermal properties through the 3ω method. *a* and *c* are the half-widths of the heater and sensor pads, both of length *b*.

$$T(x, y, t) = \psi(x, y) + \text{Re}\left(\theta(x, y)e^{2i\omega t}\right), \tag{3}$$

where ψ and θ are the steady-state and modulated components of temperature. The real and imaginary parts of θ are the signals measured by the 3ω method, and, therefore, we are going to focus on its determination from now on. After inserting Eq. (3) into Eq. (1), one obtains

$$k_{\parallel}\frac{\partial^2 \theta}{\partial x^2} + k_{\perp}\frac{\partial^2 \theta}{\partial y^2} = 2i\omega C\theta. \tag{4}$$

Equation (4) can be solved by using the method of separation of variables, which, along with Eqs. (2b)–(2d), yields

$$\theta_1 = \sum_{n=0}^{\infty} A_n\left[\gamma_n \sinh(S_{1n}(d - y)) + \chi_n \cosh(S_{1n}(d - y))\right] \times \cos(\lambda_n x), \tag{5a}$$

$$\theta_2 = \sum_{n=0}^{\infty} A_n e^{-S_{2n}(y-d)} \cos(\lambda_n x), \tag{5b}$$

where $\gamma_n = k_{2\perp}S_{2n}/(k_{1\perp}S_{1n})$, $\chi_n = 1 + Rk_{2\perp}S_{2n}$, $\lambda_n L = (n + 1/2)\pi$,

$S_{mn}^2 = (k_{m\parallel}/k_{m\perp})(\lambda_n^2 + 2i\omega/\alpha_{m\parallel})$, and $\alpha_{m\parallel} = k_{m\parallel}/C_m$ is the in-plane thermal diffusivity of the material m. The values of λ_n were determined by imposing the condition $T_n(L, y, t) = T_0$, which is well satisfied for samples with long lateral dimensions. The combination of Eqs. (2a) and (5a) together with the orthogonality of the functions $\cos(\lambda_n x)$, for $n = 0, 1, 2, \ldots$, provides the following expression for the parameter A_n:

$$A_n = \frac{P_0}{bL}\frac{\sin(\lambda_n a)}{\lambda_n a}\frac{1}{k_{1\perp}S_{1n}F_n + hG_n}, \tag{6a}$$

$$F_n = \gamma_n \cosh(S_{1n}d) + \chi_n \sinh(S_{1n}d), \tag{6b}$$

$$G_n = \gamma_n \sinh(S_{1n}d) + \chi_n \cosh(S_{1n}d), \tag{6c}$$

where $P_0 = 0.5R_0I_0^2$ is the amplitude of the injected electrical power. As the film length is considered to be long, the difference $\lambda_{n+1} - \lambda_n = \Delta\lambda = \pi/L \to 0$, which allows to convert the sums in Eqs. (5a) and (5b) into integrals. For the surface temperature $\theta_1(x, 0)$, this conversion yields

$$\theta_1(x, 0) = \frac{P_0}{\pi b}\int_0^\infty \frac{\sin(\lambda a)}{\lambda a}\frac{\cos(\lambda x)d\lambda}{k_{1\perp}S_1F/G + h}, \tag{7}$$

where $F = F_n(\lambda_n \to \lambda)$, $G = G_n(\lambda_n \to \lambda)$, and $S_m = S_{mn}(\lambda_n \to \lambda)$. According to Fig. 1 and Eq. (7), the measurable temperature fluctuations of the heater (T_h) and sensor (T_s) pads are given by the following averages:

$$T_h = \frac{1}{2a}\int_{-a}^{a}\theta_1(x, 0)dx = \frac{P_0}{\pi b}\int_0^\infty \left(\frac{\sin(\lambda a)}{\lambda a}\right)^2 \frac{d\lambda}{k_{1\perp}S_1F/G + h}, \tag{8a}$$

$$T_s = \frac{1}{2c}\int_{l+a}^{l+a+2c}\theta_1(x, 0)dx = \frac{P_0}{\pi b}\int_0^\infty \frac{\sin(\lambda a)}{\lambda a}\frac{\sin(\lambda c)}{\lambda c}\frac{\cos(\lambda(l + a + c))d\lambda}{k_{1\perp}S_1F/G + h}. \tag{8b}$$

In terms of the dimensionless integration parameter $\xi = \lambda a$, Eqs. (8a) and (8b) can conveniently be rewritten as follows:

$$T_h = T_c\int_0^\infty \left(\frac{\sin(\xi)}{\xi}\right)^2 \frac{d\xi}{\chi\sqrt{\xi^2 + z_2^2} + B_i}, \tag{9a}$$

$$T_s = T_c\int_0^\infty \frac{\sin(\xi)}{\xi}\frac{\sin(\xi c/a)}{\xi c/a}\frac{\cos(\beta\xi)d\xi}{\chi\sqrt{\xi^2 + z_2^2} + B_i}, \tag{9b}$$

where the characteristic temperature $T_c = P_0/(\pi b\bar{k}_2)$, $\bar{k}_2 = \sqrt{k_{2\parallel}k_{2\perp}}$ is the harmonic average of the substrate thermal conductivities, $B_i = ha/\bar{k}_2$ is the Biot number, $\beta = 1 + (l + c)/a$, and

$$\chi = \frac{1 + (1 + \rho\sigma_2)\Gamma^{-1}\tanh\left(\sigma_1\sqrt{k_{1\parallel}/k_{1\perp}}d/a\right)}{1 + \rho\sigma_2 + \Gamma\tanh\left(\sigma_1\sqrt{k_{1\parallel}/k_{1\perp}}d/a\right)}, \tag{10}$$

where $\rho = R\bar{k}_2/a$, $\sigma_m = \sqrt{\xi^2 + z_m^2}$, $z_m = \sqrt{if/f_m}$, $f_m = \alpha_{m\parallel}/(2\pi a^2)$, and $\Gamma = \bar{k}_2\sigma_2/(\bar{k}_1\sigma_1)$. Equations (9) and (10) thus establish that the heater and sensor temperatures depend on the product $k_{1\parallel}k_{1\perp} = \bar{k}_1^2$ and ratio $k_{1\parallel}/k_{1\perp}$ of the film thermal conductivities via the parameter Γ and the hyperbolic tangent, respectively. Since the integrants in Eqs. (9a) and (9b) are even functions, they can conveniently be integrated by using the Fourier transform method. Recalling that the Fourier transform $\tilde{F}(\lambda)$ of the function $F(x)$ is defined by $\tilde{F}(\lambda) = \int_{-\infty}^{\infty}F(x)e^{-i\lambda x}dx$, such that $F(x) = (2\pi)^{-1}\int_{-\infty}^{\infty}\tilde{F}(\lambda)e^{i\lambda x}d\lambda$, the integral $I_1 = \int_0^\infty g(x)dx$ of an even function $g(x) = g(-x)$ is given by $I_1 = 0.5\int_{-\infty}^{\infty}g(x)dx = \tilde{g}(0)/2$. Similarly, the integral $I_2 = \int_0^\infty g(x)\cos(\beta x)dx = 4^{-1}\int_{-\infty}^{\infty}g(x)\left(e^{i\beta x} + e^{-i\beta x}\right)dx = 0.5\int_{-\infty}^{\infty}g(x)e^{-i\beta x}dx = \tilde{g}(\beta)/2$. These results thus establish the following identities for the integral of an arbitrary even function

$$\int_0^\infty g(x)dx = \frac{1}{2}\tilde{g}(0), \tag{11a}$$

$$\int_0^\infty g(x)\cos(\beta x)dx = \frac{1}{2}\tilde{g}(\beta). \tag{11b}$$

For the sake of simplicity, we are going to apply Eqs. (11a) and (11b) to integrate the integrals in Eqs. (9a) and (9b) by considering that $c = a$ and the following particular cases.

A. Anisotropic substrate with negligible radiative losses

According to Eqs. (9a) and (9b), the 3ω temperature fields of the heater and sensor pads on a bare anisotropic substrate ($d = 0 = R$ and hence $\chi = 1$) with negligible radiative losses ($B_i = 0$), are given by

$$T_h = T_c\int_0^\infty \left(\frac{\sin(\xi)}{\xi}\right)^2 \frac{d\xi}{\sqrt{\xi^2 + z_2^2}}, \tag{12a}$$

$$T_s = T_c\int_0^\infty \left(\frac{\sin(\xi)}{\xi}\right)^2 \frac{\cos(\beta\xi)d\xi}{\sqrt{\xi^2 + z_2^2}}. \tag{12b}$$

Equations (12a) and (12b) indicate that both the heater and sensor signals of the 3ω method can be used to determine the harmonic average of the thermal conductivity ($\bar{k}_2$) and the in-plane thermal diffusivity ($\alpha_{2\parallel}$) involved in the parameters $Tc = P_0/(\pi b\bar{k}_2)$ and $f_2 = \alpha_{2\parallel}/(4\pi a^2)$ ($z_2 = \sqrt{if/f_2}$) of an anisotropic substrate. The 3ω signal, therefore, cannot be used to determine the cross-plane thermal conductivity of an anisotropic substrate via T_c, as is usually misconceived. By contrast, for an isotropic substrate ($k_{2\parallel} = k_{2\perp}$),

Eq. (12a) reduces to the standard model of the 3ω method for bulk materials.

To apply Eqs. (11a) and (11b) to integrate the integrals in Eqs. (12a) and (12b), we consider that $g(\xi) = g_1(\xi)g_2(\xi)$, with $g_1(\xi) = (\sin(\xi)/\xi)^2$ and $g_2(\xi) = \left(\xi^2 + z_2^2\right)^{-1/2}$. The Fourier transforms of these functions are $\tilde{g}_1(\lambda) = (\pi/4)(|\lambda+2| + |\lambda-2| - 2|\lambda|)$ and $\tilde{g}_2(\lambda) = 2K_0(z_2|\lambda|)$, with K_0 being the modified Bessel function of second kind and order zero. According to the convolution theorem, the Fourier transform of $g(\xi)$ is then given by $\tilde{g}(\lambda) = (2\pi)^{-1}\int_{-\infty}^{\infty}\tilde{g}_1(\lambda')\tilde{g}_2(\lambda-\lambda')d\lambda'$, which yields

$$\tilde{g}(\lambda) = \frac{1}{2}\left[\int_{-2}^{0}(2+\lambda') + \int_{0}^{2}(2-\lambda')\right]K_0(z_2|\lambda-\lambda'|)d\lambda'. \tag{13}$$

The combination of Eqs. (11) and (12) then establishes that $T_h/T_c = 0.5\tilde{g}(0)$ and $T_s/T_c = 0.5\tilde{g}(\beta)$, for $\beta = 2 + l/a > 2$. According to Eq. (13), these results can be simplified and explicitly be written as follows:

$$\frac{T_h}{T_c} = 2\int_0^1 (1-\xi)K_0(2z_2\xi)d\xi, \tag{14a}$$

$$\frac{T_s}{T_c} = \int_0^1 (1-\xi)[K_0(z_2(\beta+2\xi)) + K_0(z_2(\beta-2\xi))]d\xi. \tag{14b}$$

The integrals in Eqs. (14a) and (14b) are fully equivalent to the corresponding ones in Eqs. (12a) and (12b) and have the advantage that they can now be integrated analytically by using the following identities $\int xK_0(yx)dx = -(x/y)K_1(xy)$ and $\int K_0(yx)dx = (\pi x/2)N(xy)$, where $N(u) = K_0(u)L_{-1}(u) + K_1(u)L_0(u)$, with K_n and L_n being the modified Bessel function of second kind and the modified Struve function of order n, respectively. In terms of these well-implemented functions in major calculation software, Eqs. (14a) and (14b) take the forms

$$\frac{T_h}{T_c} = \pi N(2z_2) + \frac{2z_2K_1(2z_2) - 1}{2z_2^2}, \tag{15a}$$

$$\frac{T_s}{T_c} = \frac{\pi}{8}\left[\beta_+^2 N(z_2\beta_+) + \beta_-^2 N(z_2\beta_-) - 2\beta^2 N(z_2\beta)\right] + \frac{1}{4z_2}\left[\beta_+ K_1(z_2\beta_+) + \beta_- K_1(z_2\beta_-) - 2\beta K_1(z_2\beta)\right], \tag{15b}$$

where $\beta_\pm = \beta \pm 2$. Equation (15a) is equivalent to the solution found by Duquesne *et al.*[24] in terms of the Meijer *G*-function and together with Eq. (15b) provides a model to fit 3ω experimental data for any modulation frequency, avoiding numerical integration and low-frequency approximations that may lead to the inaccurate determination of the material thermal properties. Taking into account that the thermal diffusivity of a great variety of solids is within the interval $(1-100)\,\mathrm{mm^2 s^{-1}}$, the characteristic frequency $f_c = \alpha_{2\|}/(4\pi a^2) \sim (0.8-80)\,\mathrm{kHz}$, for the typical value of the sensor half-width $a = 10\,\mu\mathrm{m}$. For a modulation frequency ($f \ll f_c$) much smaller than this relatively high value of f_c, the behavior of Eqs. (15a) and (15b) can conveniently be obtained by using the following series expansion of $K_0(2u) = -[\gamma + \ln(u)]I_0(2u) + u^2 + (1+1/2)z^4/(2!)^2 + (1+1/2+1/3)z^6/(3!)^2 + \cdots$, where $I_0(2u) = 1 + u^2 + z^4/(2!)^2 + z^6/(3!)^2 + \cdots$ and $\gamma = 0.5772\ldots$ is the Euler gamma constant. After inserting this expansion of K_0 into Eq. (14a) and integrating term by term, one obtains

$$\frac{T_h}{2T_c} = \sum_{n=0}^{\infty}\frac{\varphi_n(if/f_c)^n}{(2n+1)(2n+2)} = \frac{\varphi_0}{1\cdot 2} + \frac{\varphi_1}{3\cdot 4}\frac{if}{f_2} + \cdots, \tag{16}$$

where the coefficients φ_n are given by

$$\varphi_0 = 1 + \frac{1}{2} - \gamma - \frac{1}{2}\ln\left(\frac{if}{f_2}\right), \tag{17a}$$

$$\varphi_n = 1 + \frac{1}{2} + \frac{1}{3} + \cdots + \frac{1}{n} - \frac{1}{(n!)^2}\left[\frac{1}{2n+1} + \frac{1}{2n+2} - \gamma - \frac{1}{2}\ln\left(\frac{if}{f_2}\right)\right], \tag{17b}$$

for $n = 1, 2, \ldots$. The zero-order approximation φ_0 thus exhibits a logarithmic dependence on frequency and is extensively used to determine the thermal conductivity of bulk materials.[4,24,25] This low-frequency approximation ($f \ll f_2$) is particularly suitable for the real part of T_h, as its first correction is proportional to $(f/f_2)^2$, given that the linear dependence on frequency is purely imaginary, as established by Eq. (16). Similarly, the zero-order approximation of the sensor signal T_s in Eq. (15b) is given by

$$T_s = \frac{3}{2} - \gamma - \frac{1}{2}\ln\left(\frac{if}{f_c}\right) - D(\beta), \tag{18a}$$

$$D(\beta) = \frac{\beta_+^2}{8}\ln(\beta_+) + \frac{\beta_-^2}{8}\ln(\beta_-) - \frac{\beta^2}{4}\ln(\beta) - \ln(2). \tag{18b}$$

The sensor signal, thus, exhibits the same logarithmic frequency dependence than the heater one (for a zero-order approximation), such that their difference $D(\beta)$ is fully determined by the ratio $\beta = 2 + l/a$ between the heater-sensor distance and the sensor half-width. The function $D(\beta)$ increases monotonically with $\beta > 2$ and takes its minimum value $D(2) = 2\ln(2)$.

B. Anisotropic substrate with radiative losses

Here, we consider that the substrate is subject to temperatures much higher than its environment and hence the radiative losses are expected to be significant. In this case, Eqs. (9a) and (9b) reduce to the following expressions (with $d = 0 = R$ and hence $\chi = 1$):

$$T_h = T_c\int_0^\infty \left(\frac{\sin(\xi)}{\xi}\right)^2 \frac{d\xi}{B_i + \sqrt{\xi^2 + z_2^2}}, \tag{19a}$$

$$T_s = T_c\int_0^\infty \left(\frac{\sin(\xi)}{\xi}\right)^2 \frac{\cos(\beta\xi)d\xi}{B_i + \sqrt{\xi^2 + z_2^2}}. \tag{19b}$$

Equation (19a) is consistent with a previous model derived by Cahill[4] for an isotropic bulk material and along with Eq. (19b) indicates that temperature profiles of the heater and sensor decrease as the radiative losses increase, as expected. In contrast to the lossless case ($B_i = 0$), both 3ω signals of a lossy substrate do not diverge in the quasi-steady-state regime ($f/f_c \to 0$), but rather they reach frequency-independent plateaus given by ($z_2 \to 0$)

$$\frac{T_{h,s}}{T_c} = \int_0^\infty \left(\frac{\sin(\xi)}{\xi}\right)^2 \frac{d\xi}{B_i + \xi}, \tag{20a}$$

$$\frac{T_{s,s}}{T_c} = \int_0^\infty \left(\frac{\sin(\xi)}{\xi}\right)^2 \frac{\cos(\beta\xi)d\xi}{B_i + \xi}, \tag{20b}$$

where the second sub-index "s" of T stands for the quasi-steady-state regime. The integrals in Eqs. (20a) and (20b) can be expressed in terms of the sine ($S_i(u) = \int_0^u \sin(x)dx/x$) and cosine ($C_i = -\int_u^\infty \cos(x)dx/x$) integral functions that are well-implemented in many computation software. Taking into account that $\beta > 2$, one obtains

$$2B_i^2 \frac{T_{h,s}}{T_c} = \pi\left(B_i - \frac{1}{2}\sin(2B_i)\right) - \gamma - \ln(2B_i) + S(2B_i) + C(2B_i), \tag{21a}$$

$$\begin{aligned} 4B_i^2 \frac{T_{s,s}}{T_c} = {} & S(B_i\beta_+) + S(B_i\beta_-) - 2S(B_i\beta) + C(B_i\beta_+) \\ & + C(B_i\beta_-) - 2C(B_i\beta) - \frac{\pi}{2}\left[\sin(B_i\beta_+) + \sin(B_i\beta_-)\right. \\ & \left. - 2\sin(B_i\beta)\right] + \ln\left(\frac{\beta^2}{\beta^2 - 4}\right), \end{aligned} \tag{21b}$$

where $S(u) = \sin(u)S_i(u)$ and $C(u) = \cos(u)C_i(u)$. Given that the thermal conductivity of a wide variety of solids falls inside the interval $(0.1-500)\,\mathrm{W m^{-1} K^{-1}}$, the maximum ($\varepsilon = 1$) Biot number $B_i = 4a\sigma T_0^3/\bar{k}_2 \sim (0.01-61) \times 10^{-5}$, for a typical value of the sensor half-width $a = 10\,\mu\mathrm{m}$ and $T_0 = 300\,\mathrm{K}$. The Biot number for the 3ω material configuration is thus expected to be much smaller than unity, which allows to well determine $T_{h,s}$ and $T_{s,s}$ in Eqs. (21a) and (21b) via their corresponding linear approximations on B_i. This first-order approximation yields

$$\frac{T_{h,s}}{T_c} \approx \frac{3}{2} - \gamma - \ln(2B_i) + \frac{\pi}{3}B_i, \tag{22a}$$

$$\frac{T_{s,s}}{T_c} \approx \frac{3}{2} - \gamma - \ln(2B_i) + \frac{\pi}{2}\beta B_i - D(\beta), \tag{22b}$$

where $D(\beta)$ is defined in Eq. (18b). The simple system of Eqs. (22a) and (22b) could, thus, be used to determine both the Biot number B_i and $\bar{k}_2$ [via $T_c = P_0/(\pi b\bar{k}_2)$] by using the very-low-frequency plateaus of the heater or sensor temperatures.

C. Anisotropic nanofilm with radiative losses and interface thermal resistance

Taking into account that the major contribution to the integrals in Eqs. (9a) and (9b) arises from $\xi \to 0$, they can significantly be simplified for a thin film with thickness much smaller than the heater half-width ($d \ll a$), thermal conductivity much smaller than that of the substrate ($\bar{k}_1 \ll \bar{k}_2$), and low modulation frequencies ($f \ll f_1$), as is usually the case of practical interest. Under these three conditions $\Gamma^{-1}\tanh\left(\sigma_1\sqrt{k_{1\parallel}/k_{1\perp}}d/a\right) \approx \left(k_{1\parallel}/\bar{k}_2\right)(d/a)\sigma_1^2/\sigma_2 \to 0$, $\Gamma\tanh\left(\sigma_1\sqrt{k_{1\parallel}/k_{1\perp}}d/a\right) \approx \left(\bar{k}_2/k_{1\perp}\right)(d/a)\sigma_2$, and, therefore, Eq. (10) reduces to $\chi^{-1} \approx 1 + \eta\sigma_2$, where the dimensionless parameter $\eta = \bar{k}_2 d/(k_e a)$ and the effective cross-plane thermal conductivity (k_e) of the nanofilm is defined by $d/k_e = R + d/\bar{k}_{1\perp}$. For this nanofilm approximation of χ, $\eta B_i = hd/k_e \ll 1$, the expression $(\chi\sigma_2 + B_i)^{-1} \approx \eta + (\sigma_2 + B_i)^{-1}$, and, therefore, Eqs. (9a) and (9b) take the forms

$$T_h(d) \approx T_h(0) + \frac{P_0 d}{2abk_e}, \tag{23a}$$

$$T_s(d) \approx T_s(0), \tag{23b}$$

where $T_h(0)$ and $T_s(0)$ are the temperature signals generated by the bare substrate, and, therefore, they are, respectively, given by Eqs. (19a) and (19b), whose solutions are obtained in Subsections II A and II B. Equations (23a) and (23b) are valid for a log-linear approximation on frequency [up to $\ln(f/f_1)$] and a quadratic one on the film thickness [up to $(d/a)^2$]. Considering the typical thermal conductivity $[(0.1-500)\,\mathrm{W m^{-1} K^{-1}}]$ and thermal diffusivity $[(1-100)\,\mathrm{mm^2 s^{-1}}]$ of solids, the numerical evaluation of the approximate Eqs. (23a) and (23b) and of their respective exact counterparts in Eqs. (9a) and (9b) shows a deviation smaller than 1% for nanofilms thinner than 300 nm and a heater half-width $a = 10\,\mu\mathrm{m}$. Equation (23a), thus, represents an accurate approximation and indicates that the nanofilm behaves as a thermal resistance d/k_e independent of the modulation frequency. The effective thermal conductivity $k_e = k_{1\perp}/(1 + Rk_{1\perp}/d) < k_{1\perp}$ can, therefore, be determined from the temperature drop $T_h(d) - T_h(0)$ across the film, provided that the substrate thermal properties [and hence $T_h(0)$] are known or determined via the sensor signal given by Eq. (23b). This methodology based on two metal pads to simultaneously measure the substrate and film thermal properties was applied by Alvarez-Quintana and Rodriguez-Viejo[26] for determining the cross-thermal conductivity of a-SiO_2 and a-SiN_x films. Therefore, the integrated models in Eqs. (23a) and (23b) are expected to facilitate the application of the two-pad methodology and avoid the need of two samples with identical substrates (with and without the film) to determine the film thermal properties. Equation (23a) can thus be used to retrieve k_e only (a combination of $k_{1\perp}$ and R) and reduces to a previous expression derived in absence of interface thermal resistance and radiative losses.[5,6,27] The fact that Eq. (23b) is independent of the nanofilm properties is reasonable as the sensor signal is expected to be more sensitive to the lateral heat conduction, which is dominated by the substrate, for the considered high thermal conductivity limit

($\bar{k}_2 \gg \bar{k}_1$) and low frequency regime. If the sensor signal is not available to determine the substrate thermal properties required to calculate $T_h(0)$, its evolution with the modulation frequency can be measured through the 3ω signal for a heater deposited on the bare substrate. As the measurements with and without the nanofilm might be done with different electrical powers and/or heater dimensions, Eq. (23a) has to be replaced by

$$\frac{d}{k_e} = \left(\frac{2abT_h}{P_0}\right)_{f+s} - \left(\frac{2abT_h}{P_0}\right)_s, \tag{24}$$

where the subscripts "f" and "s" stand for film and substrate, respectively. The difference in Eq. (24) is thus independent of the substrate properties and modulation frequency. In practice, however, the right-hand side of Eq. (24) may still depend on frequency due to experimental uncertainty, and hence, its average value has to be used for determining k_e.[6,7]

III. RESULTS AND DISCUSSIONS

The real and imaginary parts (or amplitude and phase) of the heater and sensor temperatures are now graphically and comparatively analyzed as functions of the modulation frequency.

Figure 2 shows the normalized real and imaginary components of the heater and sensor temperatures for a bulk (semi-infinite) material, as functions of the modulation frequency. For low frequencies ($f \ll f_2$), Re(T_h) and Re(T_s) exhibit a log-linear dependence on frequency and they are well described by their corresponding zero-order approximations (dashed lines) predicted by Eqs. (17a) and (18a), respectively. As the frequency increases, both Re(T_h) and Re(T_s) decreases until vanishing for high enough frequencies ($f \gg f_2$). This is also the case of Im(T_h) and Im(T_s), which monotonically increase with frequency and saturate at $-\pi/4$, for low enough frequencies. The real and imaginary parts of T_s thus exhibit pretty much the same behavior than the corresponding ones of T_h, but at lower frequencies. This frequency shift downward increases with β and indicates that the sensor temperature requires

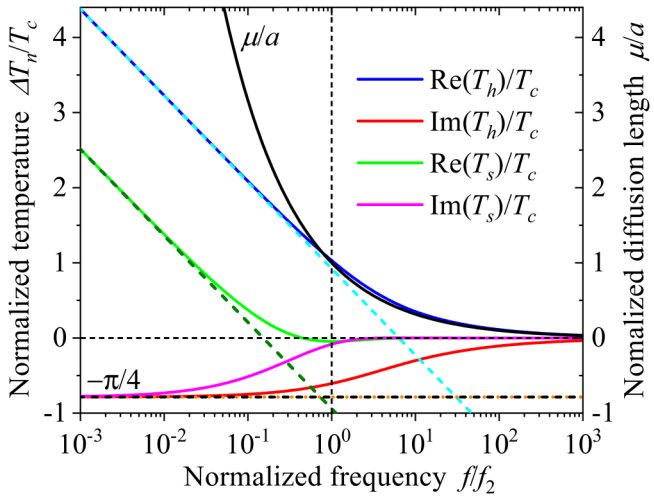

FIG. 2. Normalized real and imaginary parts of the temperature fields of the heater and sensor pads on top of a bulk material, as functions of the normalized modulation frequency. The dashed lines stand for the zero-order approximations predicted by Eqs. (17a) and (18a), and the continuous black line represents the diffusion propagation length $\mu = a\left(\sqrt{f/f_2}\right)^{-1}$. Calculations were done for $B_i = 0$ and $\beta = 3$ ($l = a$), which is chosen to keep the sensor signal observable and emulate our experimental conditions described below.

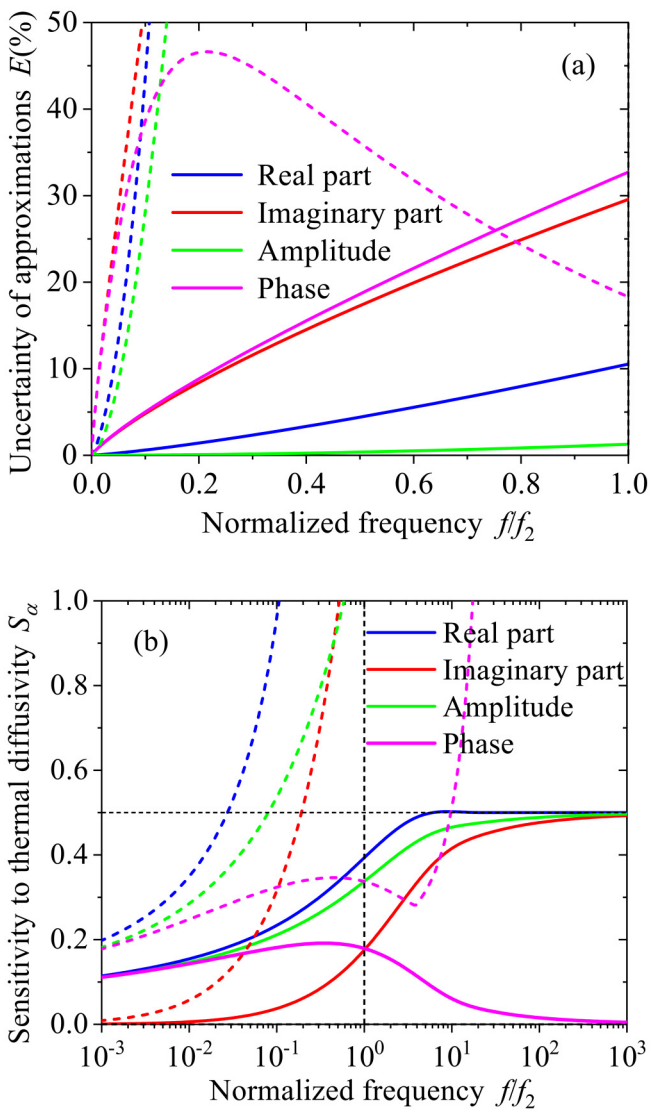

FIG. 3. Frequency spectrum of the (a) uncertainty of the zero-order approximation and (b) sensitivity of the exact 3ω signals to the in-plane thermal diffusivity of a bulk material. Calculations were done for the real and imaginary parts, as well as the amplitude and phase of the heater (solid lines) and sensor (dashed lines) temperatures. The parameters $\beta = 3$ and $B_i = 0$ were used.

lower frequencies than the heater one to determine the material thermal properties. The relatively low-frequency dependence of T_s, thus, represents an advantage of the sensor pad as the 3ω signal is usually recorded with more accuracy at low frequencies.[6]

As the zero-order approximations of T_h and T_s in Eqs. (17a) and (18a) are commonly used to determine the material thermal conductivity, their deviations from the exact solutions in Eqs. (15a) and (15b) are of practical interest. The uncertainty $E = |1 - S_a/S| \times 100\%$ of this low-frequency approximation ($f < f_2$) is shown in Fig. 3(a) for the real and imaginary parts as well as the amplitudes and phases of T_h and T_s. S_a and S represent the respective approximate and exact values of one of these four 3ω signals. Note that the components of T_h (solid lines) generally exhibit smaller derivations that those of T_s (dashed lines) such that E(amplitude) < E(realpart) < E(imaginarypart) < E(phase). The zero-order approximation of the amplitude of T_h is, therefore, expected to yield more accurate results than its real part, whose derivation from the exact solution tends to 10%, for $f \to f_2$. This relatively small uncertainty of the amplitude is particularly important for the determination of the thermal diffusivity, as the real part and amplitude of T_h have similar sensitivities to this material property, as shown in Fig. 3(b). These sensitivities $S_\alpha = |(\partial S/\partial \alpha_{2\parallel})\alpha_{2\parallel}/S| = |(\partial S/\partial \Omega)\Omega/S$ are calculated with the exact S signal and $\Omega = f/f_2$. Note that the 3ω signals of the sensor pad (dashed lines) exhibit higher sensitivities than the corresponding ones of the heater pad (solid lines), even at relatively low frequencies. This latter fact confirms the suitability of the exact sensor signal to determine the in-plane thermal diffusivity of bulk materials, due to its natural sensitivity to the in-plane heat conduction.

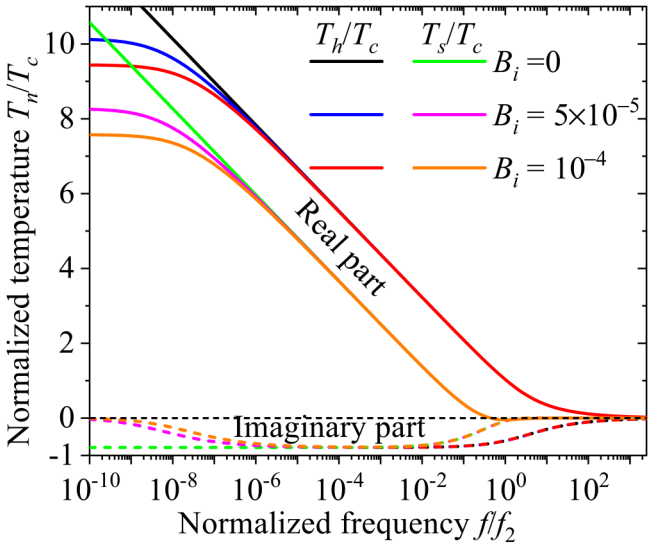

FIG. 4. Frequency evolution of normalized real (solid lines) and imaginary (dashed lines) parts of the temperature fields of the heater and sensor pads on top of a bulk material undergoing radiative losses. Calculations were done for $\beta = 3$ and two representative values of B_i.

The frequency evolution of the real and imaginary parts of the heater and sensor temperatures for a bulk material undergoing radiative losses are shown in Fig. 4, for two representatives Biot numbers. Note that in presence of radiative losses, both the heater and sensor signals are practically the same than their corresponding counterparts in absence of losses, for any frequency $f/f_2 > 10^{-5}$. As the typical values of $f_2 \sim (0.8-80)$ kHz, this inequality [$f \gtrsim (0.008-0.8)$ Hz] indicates that the radiative losses are negligible for the vast majority of frequencies used in practice, as estimated in the literature.[2,4] For lower modulation frequencies, on the other hand, the real parts deviate from their respective log-linear behavior obtained in the absence of losses and tend to a plateau, as predicted by Eqs. (22a) and (22b). This deviation increases with the Biot number and hence its observation would represent the signature of radiative losses. This signature is also present in the imaginary parts, which change their low-frequency plateau from $-\pi/4$ to zero. These plateaus of the heater and sensor signals in presence of radiative losses are similar to the ones induced by a substrate of finite thickness D. In this case, Eqs. (9) and (10) are still valid under the replacement: $\tanh(\sigma_1\sqrt{k_{1\parallel}/k_{1\perp}}d/a) \to \tanh(\sigma_1\sqrt{k_{1\parallel}/k_{1\perp}}d/a)\tanh(\sigma_2\sqrt{k_{2\parallel}/k_{2\perp}}D/a)$. This latter hyperbolic tangent related to the substrate induces a low-frequency plateau that can appear at frequencies comparable to or pretty different than those for the radiation-based one, depending on the values of the multiple properties driving their appearance.

To apply the integrated models for the heater and sensor signals, we performed 3ω measurements for a quartz glass wafer. This 500 μm-thick sample with a surface area of 1×1 cm^2 (model CRM 5809-a and number 25) was purchased from the National Metrology Institute of Japan with a calibrated thermal diffusivity for temperatures ranging from 300 to 800 K.[28] The sample of quartz glass thus allows to test and validate our model and experimental data in a broad temperature range involving high temperatures that cannot be covered with common anisotropic materials, such as the polymers PEDOT:PSS[29] and Te-PEDOT:PSS.[30] Two parallel and symmetric Cr/Pt (10/100 nm thick) wires were patterned on top of the sample by lift-off and used as the heater and sensor with a common length $b = 976\,\mu$m. The haft-widths of the heater and sensor were $a = (3.39 \pm 0.03)\,\mu$m and $c = (3.46 \pm 0.04)\,\mu$m, respectively; and their edge-to-edge distance was $l = (4.11 \pm 0.04)\,\mu$m. The measurement setup is based on a classic AC half Wheatstone bridge on the heater side and a DC Wheatstone bridge on the sensor side. The sample is loaded in a vacuum station implemented with four probe tips and operated from 300 to 827 K, which is highest temperature for a reported 3ω measurement, to be best of our knowledge. A low-noise AC current was circulated along the heater micro resistance and modulated with frequencies from 1 Hz to 80 kHz. At this highest frequency, the AC temperature rise of the two patterned micro resistances reduces to zero, and, therefore, it was used to determine their temperature coefficient of resistance (TCR). The obtained TCR values of the heater and sensor at 300 K were $(110.94 \pm 3.24) \times 10^{-5}$ K^{-1} and $(109.01 \pm 3.61) \times 10^{-5}$ K^{-1}, respectively. The electrical resistance of the pads (1×1 mm^2) and of their connections to the heater and sensor are both negligible compared to the one (150 Ω at 300 K) of these wires, which make them suitable for the 3ω

measurements. These measurements were stabilized during 10 min for each frequency, and during 60 min for each holder temperature.

Figure 5(a) shows the typical fitting of the real parts of the heater and sensor temperatures recorded by our 3ω experimental setup. We consider the fitting of the real parts only because they exhibit the highest sensitivity to the thermal conductivity and thermal diffusivity [see Fig. 3(a)] and hence allow the accurate determination of these two thermal properties. The absence of a plateau for the lower frequencies indicates that our measurements

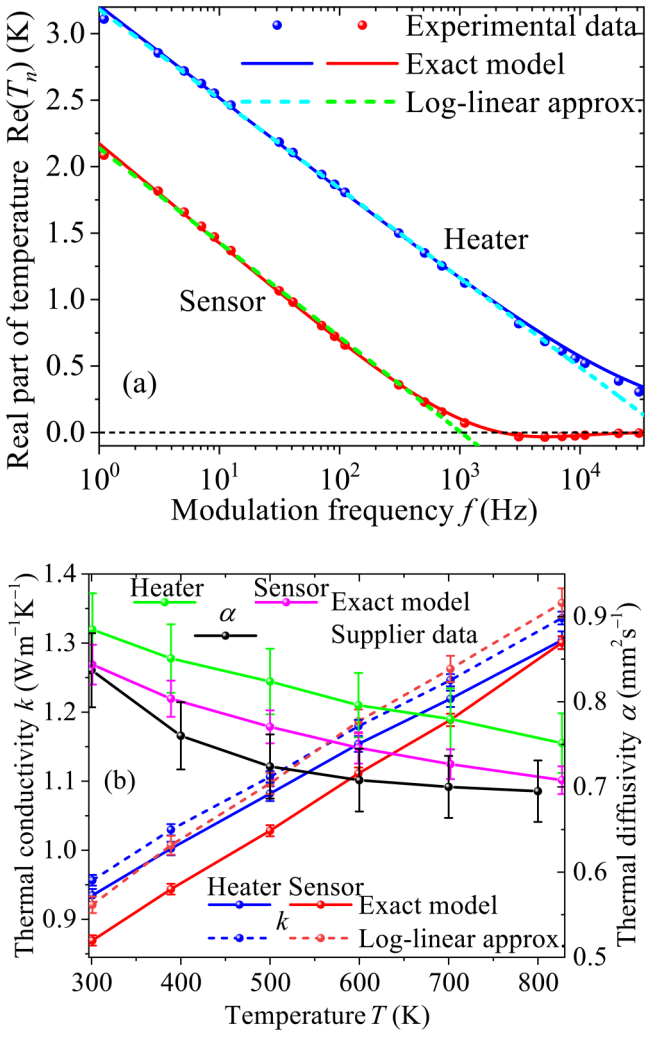

FIG. 5. (a) Typical fitting of the real parts of the heating and sensor temperatures obtained for an quartz glass wafer and (b) its corresponding fitted thermal conductivity and thermal diffusivity. The sample and its certified thermal diffusivity (supplier data) were bought from the National Metrology Institute of Japan.[28] The solid and dashed lines in (a) represent fittings with the exact models [Eqs. (15a) and (15b)] and their log-linear approximations [Eqs. (17a) and (18a)], respectively. The error bars in (b) represent the standard deviations obtained through a standard least-square fit.

are insensitive to the radiative losses, as shown in Fig. 4. Note that the exact models in Eqs. (15a) and (15b) accurately fit (solid lines) the data for all frequencies up to 31 kHz, at which the sensor signal nearly vanishes. The log-linear behavior of the heater and sensor signals at low frequency is also well fitted by their corresponding theoretical approximations in Eqs. (17a) and (18a), as shown by the dashed lines. Considering that the heater and sensor signals exhibit a well-defined log-linear profile for frequencies up to 3100 and 311 Hz, respectively; the log-linear approximation of these signals were fitted in those frequency domains via a standard least-square fit. Even though these low-frequency fittings are pretty much superposed to the corresponding ones of the exact models, they overestimate the thermal conductivity values predicted by these latter models, as shown in Fig. 5(b). This overestimation, smaller than 5% for the heater and sensor signals, is consistent with the uncertainty of the log-linear approximation of the real part, as shown in Fig. 3(a). More importantly, the thermal conductivity values fitted with the exact models for the heater and sensor signals are mutually consistent and increase with temperature, as expected for amorphous quartz glass. The deviation of the heater-extracted thermal conductivity from its sensor counterpart takes the largest value of 4% at 300 K and is explained by the absence of fitting at high enough frequencies ($>$ 31 KHz), where obtaining accurate experimental data becomes difficult. By contrast, as the sensor signal reduces to zero at lower frequencies, its fitting is complete, and, therefore, the sensor-extracted thermal conductivity values are expected to be more reliable than those retrieved from the heater signal. This is also the case of the thermal diffusivity, as the sensitivity of the real parts of the heater and sensor signals to this thermal property increases with frequency [see Fig. 3(b)]. However, the deviation of the heater-extracted thermal diffusivity from its sensor counterpart is small ($<$ 3%) and their absolute values are consistent with the ones provided by the sample supplier (black points) for temperatures ranging from 300 to 800 K.

Finally, we point out that the temperature fields considered in this work were derived by neglecting the thermal effects of the heater and sensor as well as of their interface thermal resistance with the film or substrate. Considering that the penetration depth of the generated thermal waves decreases as the modulation frequency increases, these effects may become important for high frequency and can be integrated into the model via thermal impedances, as detailed in the literature.[7,30]

IV. CONCLUSIONS

We have derived and analytically integrated over the heater and sensor widths the temperature fields of the 3ω method for anisotropic bulk materials and thin films. This integration allows to express the frequency dependence of temperature in terms of the modified Bessel and Struve functions, which are well-implemented in major computation software. We have found that (i) the usual log-linear approximation for the temperature field at low frequency is sensitive to an effective thermal conductivity of the nanofilm, which is lower than its real cross-plane thermal conductivity due to the interface thermal resistance with the substrate. (ii) For the vast majority of modulation frequencies used in practice, the 3ω signal of solid materials is nearly independent of radiative losses whose effects

may appear from frequencies lower than 1 Hz mainly. (iii) The frequency spectrum of the temperature field at a sensor pad is similar to that of the heater one, but at lower frequencies. This frequency displacement downward increases with the heater-sensor distance and could facilitate the determination of the material thermal properties due to the facility to accurately measure the temperature signal at relatively low frequencies. Further, by fitting the integrated model to our own 3ω signals recorded for modulation frequencies up to 31 KHz, the thermal conductivity and thermal diffusivity of a quartz glass wafer have been determined for temperatures ranging from 300 to 800 K. The obtained results have shown that the log-linear approximation can overestimate the thermal conductivity values by about 5%, which can be avoided with the integrated exact model.

ACKNOWLEDGMENTS

This work was supported by the CREST Japan Science and Technology Agency (Grant Nos. JPMJCR19Q3 and JPMJCR19I1) and the JSPS Kakenhi (Grant No. 21H04635). This work was also supported by the JSPS core-to-core program (Grant No. JPJSCCA20190006).

AUTHOR DECLARATIONS

Conflict of Interest

The authors have no conflicts to disclose.

Author Contributions

Jose Ordonez-Miranda: Conceptualization (equal); Data curation (equal); Formal analysis (equal); Validation (equal). **Laurent Jalabert:** Conceptualization (equal); Methodology (equal); Software (equal); Validation (equal); Writing – original draft (equal). **Yunhui Wu:** Investigation (equal); Methodology (equal); Resources (equal). **Sebastian Volz:** Investigation (equal); Resources (equal). **Masahiro Nomura:** Funding acquisition (equal); Investigation (equal); Resources (equal); Writing – review & editing (equal).

DATA AVAILABILITY

The data that support the findings of this study are available from the corresponding author upon reasonable request.

REFERENCES

[1]O. M. Corbino, Phys. Z. **11**, 413 (1910).
[2]D. G. Cahill and R. O. Pohl, Phys. Rev. B **35**, 4067 (1987).
[3]N. O. Birge and S. R. Nagel, Rev. Sci. Instrum. **58**, 1464 (1987).
[4]D. G. Cahill, Rev. Sci. Instrum. **61**, 802 (1990).
[5]C. Dames, Annu. Rev. Heat Transf. **16**, 7 (2013).
[6]S.-M. Lee and D. G. Cahill, J. Appl. Phys. **81**, 2590 (1997).
[7]T. Borca-Tasciuc, A. R. Kumar, and G. Chen, Rev. Sci. Instrum. **72**, 2139 (2001).
[8]J. H. Kim, A. Feldman, and D. Novotny, J. Appl. Phys. **86**, 3959 (1999).
[9]T. Tong and A. Majumdar, Rev. Sci. Instrum. **77**, 104902 (2006).
[10]J. Jin, M. P. Manoharan, Q. Wang, and M. A. Haque, Appl. Phys. Lett. **95**, 033113 (2009).
[11]A. Jain and K. E. Goodson, J. Heat Transf. **130**, 102402 (2008).
[12]Y. Wu, J. Ordonez-Miranda, L. Jalabert, S. Tachikawa, R. Anufriev, H. Fujita, S. Volz, and M. Nomura, Appl. Phys. Lett. **121**, 112203 (2022).
[13]R. Prasher, T. Tong, and A. Majumdar, Nano Lett. **8**, 99 (2008).
[14]X. J. Hu, A. A. Padilla, J. Xu, T. S. Fisher, and K. E. Goodson, J. Heat Transf. **128**, 1109 (2005).
[15]I. K. Moon, Y. H. Jeong, and S. I. Kwun, Rev. Sci. Instrum. **67**, 29 (1996).
[16]C. Dames and G. Chen, Rev. Sci. Instrum. **76**, 124902 (2005).
[17]H. Wang and M. Sen, Int. J. Heat Mass Transf. **52**, 2102 (2009).
[18]J.-L. Battaglia, C. Wiemer, and M. Fanciulli, J. Appl. Phys. **101**, 104510 (2007).
[19]C. E. Raudzis, F. Schatz, and D. Wharam, J. Appl. Phys. **93**, 6050 (2003).
[20]A. T. Ramu and J. E. Bowers, J. Appl. Phys. **112**, 043516 (2012).
[21]T. Ding, Y. Jannot, and A. Degiovanni, Int. J. Therm. Sci. **86**, 314 (2014).
[22]Z.-X. Zong, Z.-J. Qiu, S.-L. Zhang, R. Streiter, and R. Liu, J. Appl. Phys. **109**, 063502 (2011).
[23]S. P. Gurrum, W. P. King, and Y. K. Joshi, J. Appl. Phys. **103**, 113517 (2008).
[24]J.-Y. Duquesne, D. Fournier, and C. Frétigny, J. Appl. Phys. **108**, 086104 (2010).
[25]W. Jaber and P.-O. Chapuis, AIP Adv. **8**, 045111 (2018).
[26]J. Alvarez-Quintana and J. Rodriguez-Viejo, Sens. Actuators A: Phys. **142**, 232 (2008).
[27]T. Yamane, N. Nagai, S.-I. Katayama, and M. Todoki, J. Appl. Phys. **91**, 9772 (2002).
[28]M. Li, M. Akoshima, and N. Yamada, Int. J. Therm. Sci. **165**, 106955 (2021).
[29]J. Liu, X. Wang, D. Li, N. E. Coates, R. A. Segalman, and D. G. Cahill, Macromolecules **48**, 585 (2015).
[30]C. Forsythe, M. P. Gordon, and J. J. Urban, J. Appl. Phys. **131**, 105109 (2022).